ACS APPLIED MATERIALS & INTERFACES

Research Article

www.acsami.org

Comparing Graphene-TiO_2 Nanowire and Graphene-TiO_2 Nanoparticle Composite Photocatalysts

Xuan Pan,[†] Yong Zhao,[†] Shu Liu,[‡] Carol L. Korzeniewski,[‡] Shu Wang,[§] and Zhaoyang Fan*[,†]

[†]Department of Electrical and Computer Engineering and Nano Tech Center, Texas Tech University, Lubbock, Texas 79409-3102, United States

[‡]Department of Chemistry and Biochemistry, Texas Tech University, Lubbock, Texas 79409-1061, United States

[§]Department of Nutrition, Texas Tech University, Lubbock, Texas 79409-1240, United States

Supporting Information

ABSTRACT: We demonstrate that uniform dispersion of TiO_2 on graphene is critical for the photocatalytic effect of the composite. The hydrothermal method was employed to synthesize TiO_2 nanowires (NW) and then fabricate graphene-TiO_2 nanowire nanocomposite (GNW). Graphene oxide (GO) reduction to graphene and hybridization between TiO_2 NWs and graphene by forming chemical bonding was achieved in a one-step hydrothermal process. Graphene-TiO_2 nanoparticle (NP) nanocomposite (GNP) was also synthesized. Photocatalytic performance and related properties of NP, NW, GNP, and GNW were comparatively studied. It was found that by incorporation of graphene, GNP and GNW have higher performance than their counterparts. More importantly, it was found that NWs, in comparison with NPs, have more uniform dispersion on graphene with less agglomeration, resulting in more direct contact between TiO_2 and graphene, and hence further improved electron−hole pairs (EHPs) separation and transportation. The adsorbability of GNW is also found to be higher than GNP. The result reveals that the relative photocatalytic activity of GNW is much higher than GNP and pure NWs or NPs.

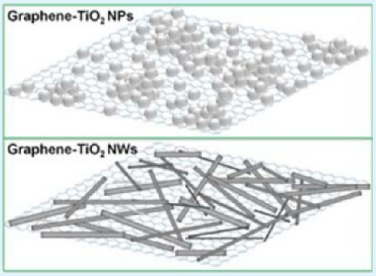

KEYWORDS: *graphene, TiO_2, nanowire, composite, photocatalyst*

1. INTRODUCTION

Graphene, in addition to its exciting electronic[1] and photonic[2] applications, is believed to be promising for energy and environment related applications,[3] such as energy storage,[4] photovoltaics,[5] photoelectrochemical[6] and photocatalytic[7,8] based water-splitting for hydrogen generation, and photocatalytic degradation[9] of organic contaminations. Considering that carbon itself has been extensively employed for different catalytic applications, graphene, the single atomic layer of graphite, with its very high electric charge carrier mobility and optical transparency, intrinsic large surface and capability of chemical functionalization, and mechanical flexibility and strength, could be an ideal mechanical support and electric charge carrier shuttle of photo sensitizers and catalysts to construct nanocomposite photocatalysts with enhanced performance based on the synergetic effects of components.[10] Furthermore, unlike electronic and photonic applications which call for high purity sp^2 bonded graphene that can only be produced by delicate approaches, energy and environment related applications require large-quantity and cost-effective methods to produce surface-functionalized and even defective single-layer or few-layer graphene, which fortunately can be easily produced through the well-known Hummer's method.[11] The resulted single or few layer graphene oxide (GO) from this method contains abundant hydrophilic groups such as hydroxyl, carboxyl, and epoxyl groups bonded with carbon and other atomic scale defects. They significantly distort sp^2 in-plane bonding and act as scattering centers that dramatically alter the optical property and electric property of graphene with low transparency, high resistivity, and low charge carrier mobility. Repairing the sp^2 aromatic structure and reduction of GO to the so-called reduced graphene oxide (RGO) is necessary to be used for charge shuttling and possible catalytic site. Chemical reduction using reducing agent such as hydrazine,[12] photochemical reduction using semiconductors,[13] and hydrothermal reduction using supercritical water[14] have been demonstrated to be effective for this purpose. The latter two "green" routes that simultaneously reduce GO and anchor semiconductor nanoparticles (NPs) on RGO are more intriguing.

With its 3.2 eV electronic band gap, TiO_2 is only sensitive to the light wavelengths below ~380 nm which belong to the UV range. Nevertheless, the cost-effective TiO_2-based materials, because of their high oxidation capability and extreme chemical stability against the strong oxidation environment in photocatalytic water-splitting and photocatalytic decontamination applications, have been the most popular photocatalysts.[15] To facilitate the use of TiO_2 powder as photocatalyst, immobilization on a suitable substrate is desired. Carbon-based materials of different origin, including activated carbon, carbon black, carbon fiber, and carbon nanotubes (CNTs), have been

Received: May 2, 2012
Accepted: July 10, 2012
Published: July 10, 2012

investigated for this purpose.[16,17] As a new member of carbon family, graphene, due to its superior properties mentioned previously, used as mechanical support and electric shuttle in composites for anchoring TiO_2 NPs has also been reported.[9,18−25] Instead of being uniformly distributed on graphene, the loaded NPs are easily accumulated along the wrinkles of graphene sheets or other defects and form agglomerations.[9] This phenomenon may dramatically reduce the synergetic catalytic effect of graphene and TiO_2 NPs. In comparison with pure TiO_2, the enhanced photocatalytic effect of CNT-TiO_2[26] and graphene-TiO_2 composites was generally attributed to three factors, including enhanced electron−hole pair separation for high quantum efficiency, extended visible light absorption for solar light harvesting, and dramatically boosted reactant adsorbability giving high reaction possibility. The heterojunction between graphene and TiO_2 promotes separation of EHPs in TiO_2 with electron injecting into graphene that acts as electron sink hindering recombination, while the hole remains in TiO_2 to drive the oxidation process. The formation of Ti−O−C bonding using carbon as dopant in TiO_2 to extend TiO_2 light absorption cutoff wavelength was also considered as one extra benefit. Unfortunately, the agglomeration of TiO_2 NPs on graphene prohibits the direct chemical contact between the two components, as illustrated in Figure 1a, and therefore will dramatically diminish these two benefits. The large surface area to easily catch the target for photo degradation, another merit of graphene, has to be discounted if TiO_2 is not uniformly distributed, since the holes in TiO_2 cannot reach those areas to oxidize the adsorbed targets. To exploit the benefits of synergistic photocatalytic effects of TiO_2 and graphene other than using graphene simply as a mechanical support, dispersion of TiO_2 on graphene with minimal agglomeration is critical.

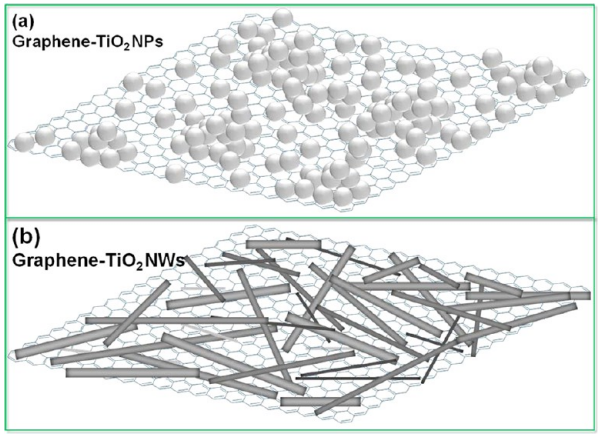

Figure 1. Schematics of (a) TiO_2 nanoparticles forming agglomerations on graphene and (b) TiO_2 nanowires dispersing uniformly on graphene. The dimensions of the components in the schematic are not in proportion.

There has been no report on the composite of TiO_2 nanowires (NWs) grafted onto graphene, called GNW here. In comparison with graphene-TiO_2 nanoparticle nanocomposite (GNP) structure, GNW composite is not a simple morphology change of TiO_2 from NP to NW. The most prominent merit to use NWs other than NPs is that NWs have a greater opportunity than NPs to be uniformly grafted onto graphene to form bonding simply based on geometric consideration, as illustrated in Figure 1b. Therefore, the photoelectron injection into graphene will occur much easier, with the potential for higher photocatalytic efficiency. Here, we report our study on the synthesis and property of GNW composite. Its superior photocatalytic capability over GNP is confirmed. It is worth emphasizing that the hydrothermal synthesis method we used guarantees that the two processes, GO reduction to RGO and the decoration of TiO_2 NPs or NWs on RGO, are implemented in the same step.

2. EXPERIMENTAL METHODS

Synthesis of TiO_2 Nanowires. A facile chemical approach was adopted to synthesize single crystalline anatase TiO_2 NWs. In a typical preparation procedure, 3 g of TiO_2 Degussa P25 nanoparticle powders (EVONIK Industries) were added into 100 mL of KOH aqueous solution (10 M) and stirred for 30 min until a homogeneous suspension was gained. A Teflon-lined autoclave (125 mL capacity) was filled with this suspension up to 80% of the total volume. Sealed into a stainless steel tank, the autoclave was kept at 200 °C for 24 h and then cooled down naturally to room temperature. The obtained products were successively washed with dilute HCl aqueous solution, deionized water, and methanol for several times until the pH value was equal to 7. After being recovered by vacuum filtration, the wet products were baked at 70 °C for 6 h, and eventually, the white-color anatase TiO_2 NW powder was obtained.

Synthesis of Graphene Oxide. Expanded flake graphite (3805, donated by Asbury Graphite Mills, Inc.) was employed for easier preparation of graphene. The expanded graphite was first oxidized into graphite oxide via modified Hummers' method. In detail, 3 g of graphite was added into a mixture of 2.5 g of $K_2S_2O_8$, 2.5 g of P_2O_5, and 12 mL of concentrated H_2SO_4. After being heated to 80 °C and kept stirring for 5 h, 500 mL of deionized water was slowly added into the mixture for dilution. Reoxidization was implemented by the addition of a large amount of deionized water (500 mL) and treated with 30% H_2O_2 solution (10 mL), causing violent effervescence and temperature increasing. By filtration through 0.22 μm Nylon film repeatedly with deionized water until the pH of the filtrate was neutral, the graphite oxide was obtained after drying the product in an oven at 60 °C for 2 h. Exfoliation was performed by sonicating 0.1 mg/mL of graphite oxide dispersion for 1 h. The graphene oxide (GO) was recovered by filtration again and vacuum drying.

Synthesis of Graphene-TiO_2 Composites. The hydrothermal method was employed to synthesize the graphene-TiO_2 nanowire GNW hybrid nanostructures, similar with the reported approach used for graphene-TiO_2 nanoparticle GNP synthesis. Thirty mg of GO was put into a solution of 90 mL of deionized water and 30 mL of ethanol under sonication for 1 h to re-exfoliate the GO thoroughly, and 3 g of as-made TiO_2 nanowires was added to the GO suspension. Then the sonication and stirring was employed alternately for 2 h with 30 min for each step until a homogeneous suspension was achieved, which shows a uniform light gray color. The suspension was then poured into a Teflon-lined autoclave of 125 mL capacity and maintained at 120 °C for 3 h to synthesize the composite of GNW, and reduction of GO was also realized during this process with ethanol as the active agent. After being cooled down to room temperature, the ultimate suspension was filtered several times with deionized water and the product was dried at ambient condition. For direct comparison, the hybrid nanostructure of GNP was also prepared according to the same procedure described above for direct comparison, in which the TiO_2 NWs were replaced with TiO_2 P25 NPs.

Characterizations. The morphology of the as-synthesized TiO_2 NWs, GNP, and GNW hybrid structures was characterized by a field-emission scanning electron microscope (FE-SEM) and transmission electron microscope (TEM). X-ray diffraction (XRD) experiments were conducted to identify the crystalline phase of TiO_2 NP, NW, GNP and GNW using a Siemens/Bruker AXS D5005 X-ray diffractometer. Measurements of Raman spectra were performed on a Bruker SENTERRA dispersive Raman microscope with excitation laser beam wavelength of 532 nm. Fourier transform infrared spectroscopy (FTIR) was also taken to verify the bonds forming

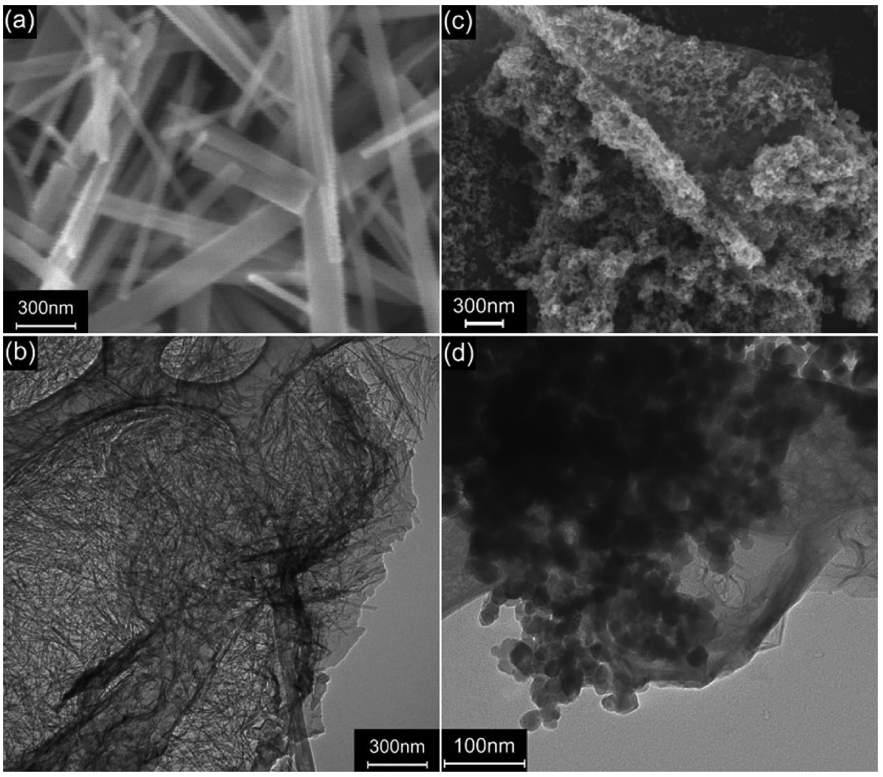

Figure 2. SEM image of TiO_2 NWs made through the hydrothermal method with KOH and TiO_2 P25 (a); (b) TEM image of the graphene-TiO_2 nanowire (GNW) hybrid nanostructures. SEM image (c) and TEM image (d) of the as-synthesized graphene-TiO_2 nanoparticle (GNP) hybrid nanostructures.

and skeletal vibration of the graphene sheets in the hybrid nanostructures. The spectrometer was a Mattson Instruments RS/1 FTIR spectrometer operating at 2 cm^{-1} resolution using a liquid nitrogen cooled MCT detector. The relative photocatalytic activities of NP, NW, GNP, and GNW were measured by the photodegradation of methylene blue (MB) under solar simulator illumination (an AM 1.5 solar simulator, Photo Emission Tech SS 50B+) with 100 mW/cm^2 intensity. Electrochemical impedance spectra (EIS) of the thin film made from these as-made materials were measured via an EIS spectrometer (EC-Lab SP-150, BioLogic Science Instruments) in a three-electrode cell by applying 10 mV alternative signal versus the reference electrode (SCE) over the frequency range of 1 MHz to 100 mHz. The cyclic voltammograms were measured in 0.1 M KCl solution containing 2.5 mM $K_3[Fe(CN)_6]/K_4[Fe(CN)_6]$ (1:1) as a redox probe with the scanning rate of 20 mV/s in the same three-electrode cell as EIS measurement. The powders of NP, NW, GNP, and GNW were fabricated into thin film electrodes via the doctor blade method on the conducting fluorine-doped SnO_2 glass substrate (FTO, TEC 15). The paste was made using acetoneacetyl (Sigma-Aldrich) and deionized water as solvent with a few drop of Triton X-100 for an even deposition. The as-made working electrodes with an area of 1 × 1 cm^2 and a film thickness around 10 μm, measured by a profilometer, were calcinated at 450 °C for 2 h in Ar atmosphere.

3. RESULTS AND DISCUSSION

Structural and Chemical Characterizations. Figure 2a shows a typical scanning electron microscope (SEM) image of the as-made titanate NWs, which was observed to be abundant in quantity and pretty tidy with smooth surface. In most previous reports on titanate 1-D nanotubes and nanowires synthesis by the hydrothermal process,[27−29] highly concentrated NaOH aqueous solution was typically used with the resulting layered tubular or rod titanate structures in a general formula, $Na_xH_{2-x}Ti_3O_7{\cdot}nH_2O$. The crystal structure is based on TiO_6 octahedra that share edges and vertices to form a 2-D framework, with sodium and hydrogen atoms filling in the interlayer space. Washing with hydrochloric acid leads to sodium-free hydrogen titanate by ion exchange reaction with the acid.[29] It is generally believed in this literature that the 1-D structure formation involves the dissolution of the starting TiO_2 3-D structure by breaking of the Ti−O−Ti bonds, rearrangement of TiO_6 octahedra into 2-D nanosheets, and nanosheets wrapping into nanotube structure at a suitable temperature range of 90−170 °C, driven by the saturation of dangling bonds.[30] If the hydrothermal temperature is higher, other morphology, including nanowires, will be formed. Here, we confirmed that the titanate NWs could be synthesized by replacing NaOH with KOH and processing at a higher temperature (200 °C). It can be noticed from the SEM image that the as-synthesized nanostructures have a length of several micrometers, but the width varies from ∼20 nm up to ∼200 nm. Particular observation indicates that the larger structure is in fact nanosheets. Figure 2b is the representative transmission electron microscope (TEM) image of hybridized GNW structure after a second hydrothermal process in the mixture of water and ethanol at 120 °C, which simultaneously reduced GO to RGO by electron donation from ethanol and formed Ti−O−C bonding between TiO_2 and RGO. Comparing panel b with panel a in Figure 2, it is noticed that the wide titanate nanosheets decomposed into very thin NWs that cover RGO surface in a reasonable uniform fashion, although occasionally, NWs are bundled together on RGO surface, indicated by the dark color area. In contrast with GNW, the SEM image in Figure 2c and TEM image in Figure 2d show that, in GNP hybrid structure, dense NPs form agglomeration on RGO. On the basis of the observation that TiO_2 NPs are

easily anchored on RGO along its wrinkles and edges,[9] it is postulated that TiO_2 is easier to form a Ti−O−C bond with RGO at the locations of defects, including functional groups. After initial anchoring of a few NPs at these locations, other NPs prefer to form agglomeration around these spots. In contrast, NWs with their significant length find more opportunities to anchor directly on RGO with less agglomeration.

Raman spectroscopy of NP, NW, GNP, and GNW was displayed in Figure 3. The Raman spectra of GNP and GNW

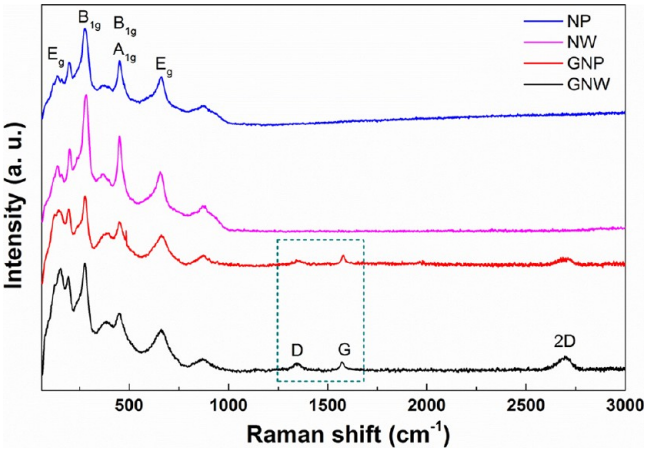

Figure 3. Raman spectra of TiO_2 P25 nanoparticles (NP), TiO_2 nanowires (NW), graphene-TiO_2 nanoparticle (GNP), and graphene-TiO_2 nanowire (GNW) hybrid nanostructures.

show the typical features of RGO with the presence of D band located at 1340 cm^{-1} and G band at 1581 cm^{-1}. G band provided information on the in-plane vibration of sp^2 bonded carbon atoms,[31] while the D band was attributed to the presence of sp^3 defects in graphene.[32] The 2D band at around 2780 cm^{-1} originated from two phonon double resonance. The Raman process shows a symmetric peak of the 2D band, which is different from that of graphite fitted with two peaks.[33] This demonstrates that the graphene has been successfully exfoliated and synthesized into the composite. The Raman lines for E_g, B_{1g}, A_{1g}, or B_{1g} modes of TiO_2 anatase phase were also observed.

X-ray diffraction (XRD) was employed for further analyzing the crystalline phase of different products as in Figure 4. The GNP showed a similar XRD pattern to the pure TiO_2 P25 NP with the typical diffraction peak (101) of anatase phase along with other peaks of (004), (200), (105), etc. and a rutile peak (110) along with other relatively weak peaks of (101), (111), (211), and (220). Furthermore, the XRD patterns of NW and GNW were also similar. It suggests that the hydrothermal process of the composite synthesis has no obvious impact on the original TiO_2 crystallization. In addition, it is worth noting that the original rutile peaks in NP were eliminated in NW and GNW, which indicates that the small fraction of rutile phase in P25 NPs has almost disappeared. No diffraction patterns from carbon species have been detected, which may result from the small amount and weak intensity of graphene.

The Fourier transform infrared spectroscopy (FTIR) transmission spectra of NP, NW, GNP, and GNW were shown in Figure 5. Both pure NP and NW showed low frequency bands around 690 cm^{-1}, which were attributed to the vibration of Ti−O−Ti. The spectra broadening below 1000 cm^{-1} in GNP and

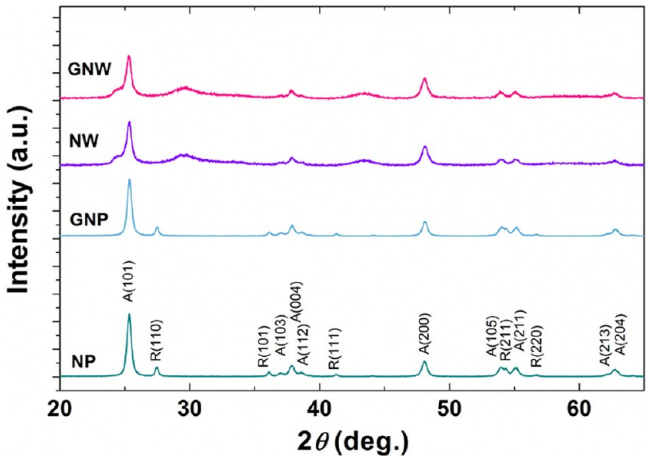

Figure 4. Representative XRD patterns of TiO_2 P25 nanoparticles (NP), TiO_2 nanowires (NW), graphene-TiO_2 nanoparticle (GNP), and graphene-TiO_2 nanowire (GNW) hybrid nanostructures. A and R refers to anatase and rutile, respectively.

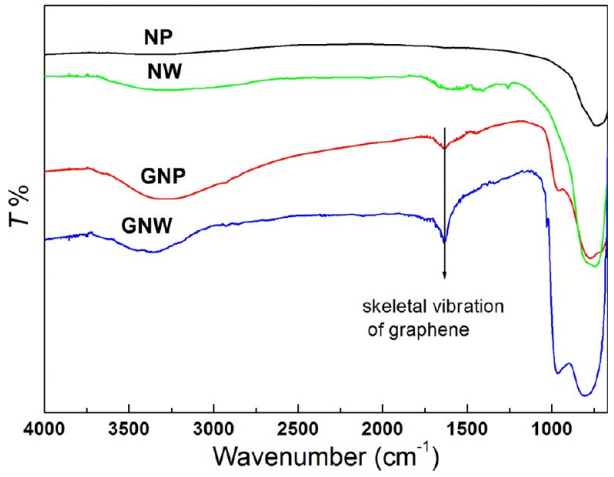

Figure 5. Fourier transform infrared (FTIR) spectra of TiO_2 P25 nanoparticles (NP), TiO_2 nanowires (NW), graphene-TiO_2 nanoparticle (GNP), and graphene-TiO_2 nanowire (GNW) hybrid nanostructures. For clear view, the background CO_2 bands (near 2300 cm^{-1}) were removed, and different spectra were shifted in the *y*-axis.

GNW, compared with the pure NP and NW was attributed to the formation of Ti−O−C bonds (798 cm^{-1}) during the hydrothermal process overlapping with the original peak of Ti−O−Ti vibration. The existence of Ti−O−C bonds confirms that the chemical bonds were firmly built between graphene and TiO_2 nanostructures. Furthermore, the observed absorption band appearing at ~1600 cm^{-1} for GNP and GNW indicates the skeletal vibration of the graphene sheets reduced from graphene oxide during the hydrothermal reaction.[9,34] In addition, the broad absorption from 3000 to 3700 cm^{-1} was caused by the O−H stretching vibration of the surface hydroxyl groups on TiO_2.

Transport Study Based on EIS and CV Measurements. One fundamental assumption to use TiO_2-graphene hybrid structure is that the heterojunction between TiO_2 and graphene will enhance the photogenerated EHPs separation with electrons from the conduction band of TiO_2 injected into graphene, while the hole trapped in TiO_2 will have a longer lifetime. Since the photocatalytic process involves the oxidation

dx.doi.org/10.1021/am300772t | ACS Appl. Mater. Interfaces 2012, 4, 3944−3950

process in which the holes transfer from photocatalysts to the degradable chemical in solution and the reduction process in which electrons transfer from the photocatalyst to the solution, the photocarriers migration in the photocatalytic solids, through the solid−solid junction and across the solid−liquid junction, will determine the reaction kinetics and rate. High conductivity of graphene renders itself as a super charge-carrier transport medium, and its large surface area may also result in higher carrier transfer rate between the photocatalyst and the solution/photodegradable chemicals. Electrochemical impedance spectroscopy (EIS) is a very useful tool to characterize the charge-carrier migration. To shed light on the charge transport performance of the different photocatalysts, EIS characterization was carried out for NP-, NW-, GNP-, and GNW-based electrodes in electrolyte containing I^-/I^{3-} as the redox couple. Figure 6 showed the EIS measurement in

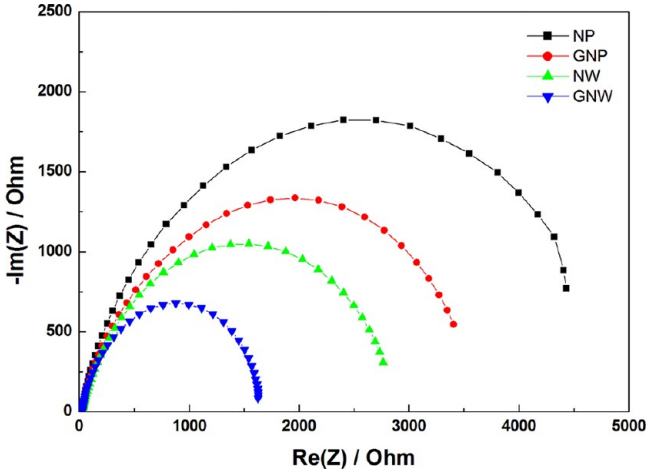

Figure 6. Nyquist plots of the EIS data of the as-made thin films on FTO glass with TiO_2 P25 nanoparticles (NP), TiO_2 nanowires (NW), graphene-TiO_2 nanoparticle (GNP), and graphene-TiO_2 nanowire (GNW) hybrid nanostructures.

Nyquist plots. Both the hybrid nanostructures of GNP and GNW showed depressed semicircles at high frequencies compared with their pure TiO_2 counterparts. The reduced semicircles indicate diminished resistance of working electrodes, suggesting a decrease in the solid state interface layer resistance and the charge transfer resistance across the solid−liquid junction on the surface by forming hybrid structures of TiO_2 with graphene .[35] In addition, the NW structure could also provide a direct path for excited electrons and suppress the carrier scattering between NPs which is a common phenomenon in a NP system. By comparison in Figure 6, NW systems are superior to NP systems with smaller semicircles, suggesting a rapid transport of charge carriers and an effective charge separation.

Figure 7 shows clear anodic and cathodic peaks for each sample. The peak at positive potentials on the anodic (forward) sweep around 0.3 V vs SCE represents the oxidation of ferrocyanide to ferricyanide with the loss of one electron. GNW and NW presented the smallest peak-to-peak separations (ΔE_p) indicating highly improved reaction reversibility. Furthermore, the hybrid structure of GNW and GNP displayed large current density. In fact, the anodic current density for GNW exhibits an enhancement of 2.4-fold compared to that of the bare NP surface, demonstrating a significantly enhanced rate of electron

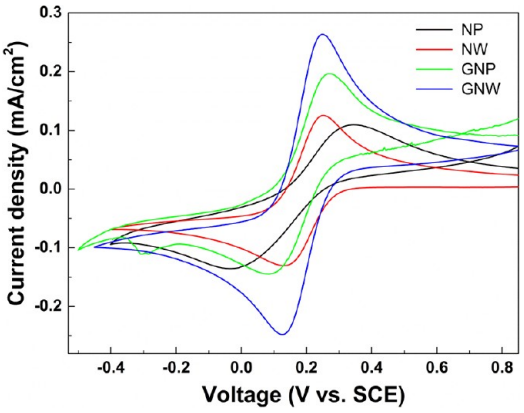

Figure 7. Cyclic voltammograms of the as-made thin films on FTO glass with TiO_2 P25 nanoparticles (NP), TiO_2 nanowires (NW), graphene-TiO_2 nanoparticle (GNP), and graphene-TiO_2 nanowire (GNW) hybrid nanostructures.

transfer attributed to the induction of the graphene as a highly conducting substrate. In addition, the NW, GNW, and GNP all show an improvement in electron transfer over the bare NP surface, which comparably exhibits sluggish kinetics.

Photocatalytic Study. Relative photocatalytic activity of each synthesized material was comparatively investigated by evaluating the photodegradation rate of MB under solar light. To measure their photodegradation rate, four Petri dishes each containing 25 mL of 2 ppm MB solution were prepared and 25 mg of each material was added. Photodegradation was measured in 10 min intervals. Special care was paid to the evaporation loss during the illumination. Therefore, the Petri dish was weighed instantly before and after exposure, and the loss was balanced by addition of distilled water. To measure the MB concentration in the solution as time elapsed under solar radiation, a small volume of solution was withdrawn and the photocatalyst powder was filtered out by 0.22 μm membranes, and then, the absorbance was measured at the wavelength of 663 nm. The concentration of MB in the solution was plotted as a function of irradiation time using Beer−Lamberts Law, and the results of different photocatalysts are displayed in Figure 8a. The changes of normalized concentration (C/C_0) of MB with irradiation were assumed to be proportional to the normalized maximum absorbance (A/A_0). It is obvious to conclude that the relative photodegradation rate of GNW and GNP hybrid nanostructures exhibited significant improvements compared to bare NP and NW. A sharp drop of MB concentration was shown at the first 10 min for GNW. This superior performance of GNP and GNW could also be confirmed according to the photographs shown in Figure 8b by comparing the color difference of the remaining MB solutions after a 40 min irradiation under solar light. It is known that the decrease of MB concentration in solution results from the physical adsorption on the photocatalyst surface and the chemical decomposition of MB. To determine the influence merely induced by adsorption, a parallel control experiment was conducted for these four photocatalysts. The same 2 ppm MB solutions with 25 mg of photocatalysts in them were kept in a dark environment for 80 min, long enough to achieve adsorption equilibrium of MB on the photocatalyst surface. Then the remaining concentration of MB in the solution was derived from adsorption measurement and plotted in Figure 8c. Apparently, GNW displays a superior adsorbability which is crucial for an efficient photocatalyst. Comparing GNW with

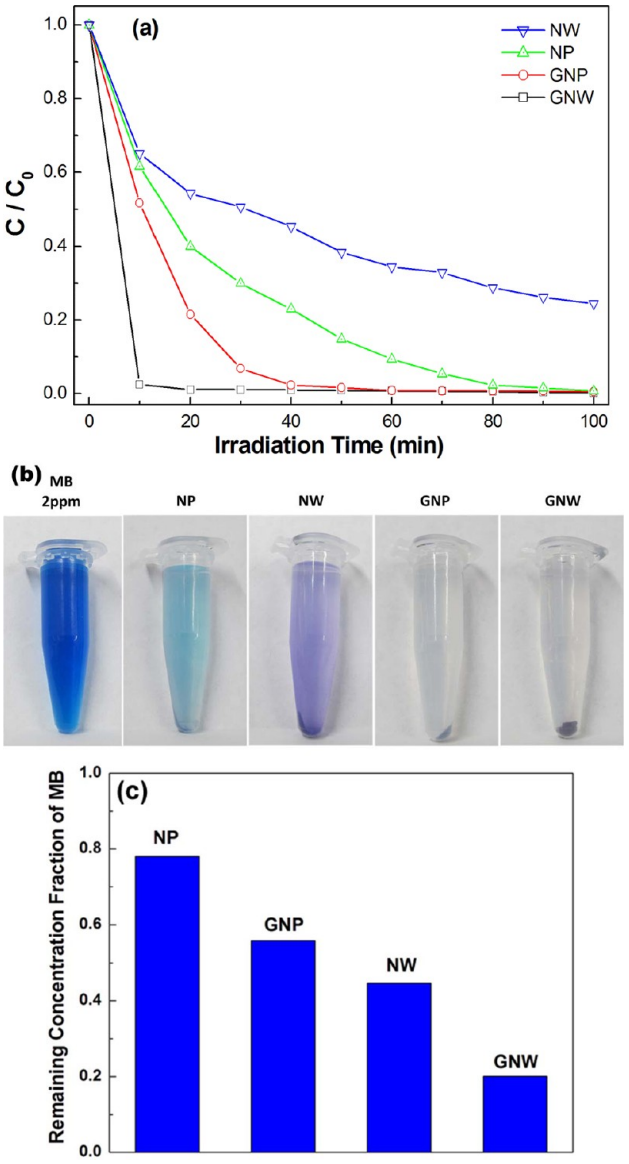

Figure 8. (a) Photodegradation of MB under solar light, where C_0 is the initial concentration of MB and C is the concentration of MB after irradiation of the sample in the corresponding time interval. (b) Photo images show the initial 2 ppm methylene blue solution and the remaining methylene blue in the solution after being irradiated under solar light for 40 min. The photos were taken after centrifugation for 10 min at a speed of 13 krpm. (c) Column plot showing the remaining MB in solution after being kept in the dark for 80 min until equilibrium of the MB concentration.

NW, the enhanced adsorbability may be attributed to two factors: (1) $\pi-\pi$ conjugation between MB and the aromatic region of 2-D RGO which certainly would lead to a strong adsorption and (2) the TiO_2 NWs morphology changed with increased surface area from the bundles in Figure 2a to the individual wires in Figure 2b after hybridization with RGO. By comparing the NP with NW in Figure 8b, the NW structure also exhibits higher capacity to trap contaminants. It is surprising that NW has larger adsorption than GNP, and the reason is unknown at the present time.

It is worth emphasizing that, in Figure 8a, the dramatic drop of MB concentration after a 10 min light radiation with GNW or GNP as photocatalyst is caused by the synergetic effects of adsorption and degradation. This can be easily identified by the observation that MB concentration is ~20% at adsorption equilibrium, while it is only ~2% after a 10 min light irradiation. Comparing graphene-TiO_2 hybrid structure with pure TiO_2, the enhanced photocatalytic activity can be attributed to the significantly enhanced EHPs separation with the electron injection into graphene to prohibit the photogenerated EHPs recombination, and the remaining hole in TiO_2 will be trapped at surface state to oxidize MB. In this oxidation process, adsorption may also indirectly enhance the reaction rate for hole transfer based on the mechanism proposed by Zhang et al.[36] In this scenario, the improved photocatalytic activity of GNW over GNP can be explained on the basis of the reaction mechanism in addition to the enhanced adsorption. As confirmed by the TEM observation in Figure 2, TiO_2 NWs have more uniform distribution on RGO than NPs, so more NWs have direct chemical bonding (electric contact) with RGO while most NPs do not. Further considering carrier transport in a straight path in a NW, in contrast with the zigzag path in agglomerated NPs, electron injection from NW to RGO will be much easier than in agglomerated NPs. As a result, the electron–hole pairs (EHPs) recombination rate in GNW will be much slower than in GNP. Moreover, the strong adsorption of MB on GNW also offers more opportunities of MB molecules close to the holes for oxidation. The synergetic effect results in a significant higher photocatalytic capability of GNW over GNP.

4. CONCLUSION

The hydrothermal method was employed to synthesize graphene-TiO_2 NPs and graphene-TiO_2 NWs hybrid nanostructures, and comparative studies were carried out to evaluate the relative photocatalytic performance of NPs, NWs, GNPs, and GNWs. By incorporating graphene, the hybrid structures have significantly higher performance over their counterparts benefiting from enhanced adsorbability of contaminants and improved photogenerated electron–hole pairs separation and transportation. More importantly, in comparison with NPs, NWs exhibit more uniform distribution on graphene with less agglomeration, resulting in more contact area between TiO_2 and graphene. The properties of both graphene and nanowire structure were validated to contribute to the enhanced charge separation and transportation. A significant improvement of graphene-TiO_2 nanowire nanostructure over other materials in the photodegradation of MB under solar light has been demonstrated, indicating that the graphene-TiO_2 nanowire hybrid nanostructure is a promising photocatalyst for remedy of environmental problems.

■ ASSOCIATED CONTENT

Supporting Information

TEM images of graphene, NW, and GNW; FTIR spectra of NP and GNP, NW and GNP at higher resolution; FITR spectra of graphene and GO; photo image of original 2 ppm MB solution and the suspensions of NP, NW, GNP, and GNW after a 40 min illumination before centrifugation; diffuse reflectance absorption spectra of NP, NW, GNP, and GNW. This material is available free of charge via the Internet at http://pubs.acs.org.

■ AUTHOR INFORMATION

Corresponding Author

*E-mail: zhaoyang.fan@ttu.edu.

Notes

The authors declare no competing financial interest.

REFERENCES

(1) Geim, A. K.; Novoselov, K. S. *Nat. Mater.* **2007**, *6*, 183.
(2) Bonaccorso, F.; Sun, Z.; Hasan, T.; Ferrari, A. C. *Nat. Photonics* **2010**, *4*, 611.
(3) Ye, Y.; Dai, Y.; Dai, L.; Shi, Z.; Liu, N.; Wang, F.; Fu, L.; Peng, R.; Wen, X.; Chen, Z.; Liu, Z.; Qin, G. *ACS Appl. Mater. Interfaces* **2010**, *2*, 3406.
(4) Zhang, K.; Han, P.; Gu, L.; Zhang, L.; Liu, Z.; Kong, Q.; Zhang, C.; Dong, S.; Zhang, Z.; Yao, J.; Xu, H.; Cui, G.; Chen, L. *ACS Appl. Mater. Interfaces* **2012**, *4*, 658.
(5) Zhu, P.; Nair, A. S.; Peng, S.; Yang, S.; Ramakrishna, S. *ACS Appl. Mater. Interfaces* **2012**, *4*, 581.
(6) Lei, Z.; Shi, F.; Lu, L. *ACS Appl. Mater. Interfaces* **2012**, *4*, 1058.
(7) Guo, S.; Dong, S. *Chem. Soc. Rev.* **2011**, *40*, 2644.
(8) Zhang, X.-Y.; Li, H.-P.; Cui, X.-L.; Lin, Y. *J. Mater. Chem.* **2010**, *20*, 2801.
(9) Zhang, H.; Lv, X.; Li, Y.; Wang, Y.; Li, J. *ACS Nano* **2010**, *4*, 380.
(10) Kamat, P. V. *J. Phys. Chem. Lett.* **2010**, *2*, 242.
(11) Hummers, W. S., Jr.; Offeman, R. E. *J. Am. Chem. Soc.* **1958**, *80*, 1339.
(12) Li, D.; Muller, M. B.; Gilje, S.; Kaner, R. B.; Wallace, G. G. *Nat. Nanotechnol.* **2008**, *3*, 101.
(13) Williams, G.; Seger, B.; Kamat, P. V. *ACS Nano* **2008**, *2*, 1487.
(14) Zhou, Y.; Bao, Q. L.; Tang, L. A. L.; Zhong, Y. L.; Loh, K. P. *Chem. Mater.* **2009**, *21*, 2950.
(15) Hashimoto, K.; Irie, H.; Fujishima, A. *Jpn. J. Appl. Phys.* **2005**, *44*, 8269.
(16) Leary, R.; Westwood, A. *Carbon* **2011**, *49*, 741.
(17) Serp, P.; Figueiredo, J. L. *Carbon materials for catalysis*; Jon Wiley & Sons, Inc.: Hoboken, NJ; 2009.
(18) Zhang, H.; Lv, X. J.; Li, Y. M.; Wang, Y.; Li, J. H. *ACS Nano* **2010**, *4*, 380.
(19) Ng, Y. H.; Lightcap, I. V.; Goodwin, K.; Matsumura, M.; Kamat, P. V. *J. Phys. Chem. Lett.* **2010**, *1*, 2222.
(20) Wang, Y.; Shi, R.; Lin, J.; Zhu, Y. *Appl. Catal., B* **2010**, *100*, 179.
(21) Zhou, K.; Zhu, Y.; Yang, X.; Jiang, X.; Li, C. *New J. Chem.* **2011**, *35*, 353.
(22) Zhu, Y.; Murali, S.; Cai, W.; Li, X.; Suk, J. W.; Potts, J. R.; Ruoff, R. S. *Adv. Mater.* **2010**, *22*, 5226.
(23) Zhang, Y.; Pan, C. *J. Mater. Sci.* **2011**, *46*, 2622.
(24) Bell, N. J.; Yun Hau, N.; Du, A.; Coster, H.; Smith, S. C.; Amal, R. *J. Phys. Chem. C* **2011**, *115*, 6004.
(25) Zhang, Y.; Tang, Z.-R.; Fu, X.; Xu, Y.-J. *ACS Nano* **2011**, *5*, 7426.
(26) Woan, K.; Pyrgiotakis, G.; Sigmund, W. *Adv. Mater.* **2009**, *21*, 2233.
(27) Kasuga, T.; Hiramatsu, M.; Hoson, A.; Sekino, T.; Niihara, K. *Adv. Mater.* **1999**, *11*, 1307.
(28) Zhang, Y. X.; Li, G. H.; Jin, Y. X.; Zhang, Y.; Zhang, J.; Zhang, L. D. *Chem. Phys. Lett.* **2002**, *365*, 300.
(29) Kolen'ko, Y. V.; Kovnir, K. A.; Gavrilov, A. I.; Garshev, A. V.; Frantti, J.; Lebedev, O. I.; Churagulov, B. R.; Van Tendeloo, G.; Yoshimura, M. *J. Phys. Chem. B* **2006**, *110*, 4030.
(30) Morgado, E.; de Abreu, M. A. S.; Moure, G. T.; Marinkovic, B. A.; Jardim, P. M.; Araujo, A. S. *Chem. Mater.* **2007**, *19*, 665.
(31) Pimenta, M. A.; Dresselhaus, G.; Dresselhaus, M. S.; Cancado, L. G.; Jorio, A.; Saito, R. *Phys. Chem. Chem. Phys.* **2007**, *9*, 1276.
(32) Zhang, W.; Cui, J.; Tao, C.-a.; Wu, Y.; Li, Z.; Ma, L.; Wen, Y.; Li, G. *Angew. Chem., Int. Ed.* **2009**, *48*, 5864.
(33) Ni, Z.; Wang, Y.; Yu, T.; Shen, Z. *Nano Res.* **2008**, *1*, 273.
(34) Wang, S.; Zhang, Y.; Abidi, N.; Cabrales, L. *Langmuir* **2009**, *25*, 11078.
(35) He, B.-L.; Dong, B.; Li, H.-L. *Electrochem. Commun.* **2007**, *9*, 425.
(36) Zhang, X. W.; Zhou, M. H.; Lei, L. *Carbon* **2005**, *43*, 1700.